Intrinsic point defects and the *n*-type dopability of Bi$_2$MoO$_6$ with higher photocatalytic performance: A hybrid functional study

Hongbin Xu [1], Dongying Li [2], Mingsen Deng [3], Xuefei Liu,[4] Zhenzhen Feng,[5] and Wentao Wang [3,*]

[1]*School of Physics and Electron Science, Guizhou Education University, Guiyang 550018, China*

[2]*Department of Environmental and Municipal Engineering, North China University of Water Conservancy and Electric Power, Zhengzhou 450011, China*

[3]*Guizhou Provincial Key Laboratory of Computational Nano-Material Science, Guizhou Education University, Guiyang 550018, China*

[4]*School of Physical and Electronic Sciences, Guizhou Normal University, Guiyang 550025, China*

[5]*Institute for Computational Materials Science, School of Physics and Electronics, International Joint Research Laboratory of New Energy Materials and Devices of Henan Province, Henan University, Kaifeng 475004, China*

Intrinsic point defects play a vital role in regulating the electronic structure and electron carrier concentration (n_0) of Bi$_2$MoO$_6$, which has been demonstrated as a promising photocatalyst. Unfortunately, the source of *n*-type conductivity for its intrinsic defects has proved challenging. Using first-principles hybrid density functional calculations, we investigate the formation energies and electronic structure of intrinsic point defects in Bi$_2$MoO$_6$. The self-consistent Fermi energies and equilibrium carrier and defect concentrations are calculated using the SC-FERMI code based on thermodynamic simulation. It is found that the easy formation of the +2 charged O vacancy (V_O^{2+}) is responsible for its intrinsic *n*-type conductivity under Bi-rich/O-poor conditions, and thus, it can have a very high density (reaching up to 10^{19} cm^{-3}), making it the dominant defect in Bi$_2$MoO$_6$. Under O-rich conditions, only adopting both D$^+$ doping and quenching methods in Bi$_2$MoO$_6$ can reach a higher carrier density ($>10^{17}$ cm^{-3}). Moreover, under the broad range of chemical potentials of -2.50 eV $< \Delta\mu_{Bi} < 0$, -6.32 eV $< \Delta\mu_{Mo} < -1.48$ eV, and -2.19 eV $< \Delta\mu_O < -0.65$ eV, after quenching from 700 to 300 K, Bi$_2$MoO$_6$ can be effectively donor doped without significant compensation, and n_0 increases as $\Delta\mu_O$ decreases or temperature increases. Our results can give a guide in selecting optimum growth and quenching conditions to achieve high *n*-type doping and suppress compensation.

I. INTRODUCTION

Bismuth molybdates are well-known photocatalysts. They have the general chemical formula Bi$_2$O$_3 \cdot n$MoO$_3$ and are divided into three types: α-Bi$_2$Mo$_3$O$_{12}$, β-Bi$_2$Mo$_2$O$_9$, and γ-Bi$_2$MoO$_6$, with *n* values of 3, 2, and 1, respectively [1], in which the γ-Bi$_2$MoO$_6$ (Bi$_2$MoO$_6$) belongs to the orthorhombic phase with the $Pca2_1$ space group. It has been primarily studied in photocatalysis [2]. This is due to the fact that Bi$_2$MoO$_6$ possesses several benefits, including chemical inertness, nontoxicity, and ideal conduction band/valence band (VB) edge orientations for visible light photocatalysis [3,4]. Furthermore, Bi$_2$MoO$_6$ has been active and selective in heterogeneous catalysis and has an excellent performance in water splitting [5] and photodegradation of numerous hardly biodegradable organic pollutants [6]. However, pure Bi$_2$MoO$_6$, on the other hand, has low efficiency in separating electrons and holes and a low quantum yield, all of which lead to its low photocatalytic activity [4]. Therefore,

the modification of Bi$_2$MoO$_6$ to enhance its photocatalytic activity is still challenging.

Recently, doping with metals [7] or nonmetals [8], inducing crystal defects [9], and developing heterojunction structures [10] have all been attempted to address the difficulties stated above. Among them, experimentally, introducing intrinsic defects (such as O, Bi, and Mo vacancies; Bi, Mo, and O interstitial; and Bi at the Mo site and Mo at the Bi site) into Bi$_2$MoO$_6$ is an efficient strategy for improving its photocatalytic efficiency [9,11–13]. For example, Huang *et al.* [11] have successfully introduced oxygen vacancy defects into Bi$_2$MoO$_6$ through a facile and fast microwave-assisted method. They found that Bi$_2$MoO$_6$ with oxygen vacancies exhibited optimum photocatalytic activity, and the degradation rate of tetracycline was 7.0 times higher than that of pure Bi$_2$MoO$_6$. This is because oxygen vacancies can create more active sites and enhance electron-hole separation. Moreover, Bi$_2$MoO$_6$ with oxygen vacancy defects is widely used in CO$_2$ photoreduction [12,14], photocatalytic NO removal [15,16], and photocatalytic degradation of organic pollutants [17,18]. For Bi defects in Bi$_2$MoO$_6$, Zhang *et al.* [9] found that the strong interaction between Bi interstitial (Bi^0) and Bi$_2$MoO$_6$ can promote electron transfer. The photogenerated holes

*wuli8@163.com

concentrated on Bi_2MoO_6 rapidly converted surface adsorbed water into highly oxidizing $\cdot$ OH and directly reacted with pollutants. It remains unclear, however, what the nature of these promoting effects is exactly. There is still a great deal of work to fully understand the photocatalytic activity induced by the intrinsic defects of Bi_2MoO_6.

On the other hand, the intrinsic defects of Bi_2MoO_6 have been studied theoretically [13,19,20]. For example, density functional theory (DFT) calculation results show that the Bi antisite (at the Mo site) defect in Bi_2MoO_6 could enhance electron excitation, promoting electron-hole separation and transmission [13], in which the generalized gradient approximation (GGA) exchange-correlation function as described by Perdew-Burke-Ernzerhof (PBE) is used. Using the same method (GGA-PBE), Di *et al.* [20] found that Bi and O vacancies codoped can tune the local geometric and electronic structure of Bi_2MoO_6. It serves as a charge separation center to boost electron-hole separation. In a recent work, Jing *et al.* [19] more systematically calculated the electronic structure and related photocatalytic properties of various native defects using the GGA-PBE method. However, the GGA-PBE method yielded significantly underestimated band gaps, i.e., 2.18 eV, compared with the experimental value of 2.53 eV [2]. Hence, quantitatively more reliable calculations are required. Moreover, the formation energies and, thus, the equilibrium concentrations of the defects depend on chemical conditions such as temperature and oxygen partial pressure, which were not considered in the previous studies [21]. All researchers mentioned above on intrinsic defects in Bi_2MoO_6 only consider the neutral state and its corresponding photocatalytic properties. Moreover, how intrinsic defects respond to and compensate for the existence of extrinsically ionized impurities, such as donors and acceptors in Bi_2MoO_6, is still open. Thus, it is necessary to gain a comprehensive understanding of its intrinsic defect properties to advance the further application of Bi_2MoO_6.

In this paper, we calculate the formation energies and electronic structure of intrinsic point defects in Bi_2MoO_6 using first-principles hybrid density functional calculations. Under Bi-rich/O-poor conditions, our results show that the easy formation of V_O^{2+} is responsible for its intrinsic *n*-type conductivity. Here, V_O^{2+} has no impurity energy band in the gap region without a recombination center of electrons and holes. Also, n_0 is $>10^{17}$ cm^{-3} with the D$^+$ doping and quenching strategy in the air environment by calculating self-consistent Fermi energies and equilibrium carrier and defect concentrations. Bi_2MoO_6 can be effectively donor doped without significant compensation by intrinsic point defect formation after quenching from 700 to 300 K, under the ranges of -2.50 eV $< \Delta\mu_{Bi} < 0$, -6.32 eV $< \Delta\mu_{Mo} < -1.48$ eV, and -2.19 eV $< \Delta\mu_O < -0.65$ eV, which agrees well with experiments. The formation of compensating acceptor defects can be inhibited by choosing oxygen-poor (Bi-rich) growth conditions and after quenching, thus providing a pathway for improved *n*-type doping.

II. COMPUTATIONAL DETAILS

First-principles calculations based on the DFT are performed using the projector-augmented wave (PAW) [22]

method implemented in the Vienna *Ab initio* Simulation Package [23,24]. The Kohn-Sham one-electron states are expanded using the plane-wave basis set with a kinetic energy cutoff of 550 eV. The PBE exchange-correlation functional within the GGA is employed for the geometrical optimization. To correct the underestimated band gap based on the PBE method, the screened hybrid functional of Heyd, Scuseria, and Ernzerhof (HSE) [25] is used to describe electronic structure accurately. The band gap of pristine Bi_2MoO_6 is tested by adjusting the Hartree-Fock mixing parameter from 0.12 to 0.25. It is found that, when $\alpha = 0.15$, the calculated band gap of Bi_2MoO_6 is 2.635 eV, like its experimental value of 2.53 eV [2]. The PAW potentials with the valence electrons $6s^2 6p^3$ for Bi, $4d^5 5s^1$ for Mo, and $2s^2 2p^6$ for O have been employed.

We adopted experimental [26,27] lattice constants $a = 5.482$ Å, $b = 16.199$ Å, $c = 5.509$ Å, and the atomic positions employed as the starting points of the partial relaxation of all ionic positions while keeping the shape-volume fixed in defecs calculations [28–30]. Our defect calculations are performed in a 144-atom (containing 96 O, 32 Bi, and 16 Mo atoms) $2 \times 1 \times 2$ supercell. The Γ-centered Monkhorst-Pack meshes [31] of k-points used for Brillouin zone sampling are $6 \times 2 \times 6$ for pure Bi_2MoO_6 unit cell calculation and $3 \times 2 \times 3$ for the intrinsic defects. It is sufficient to reach convergence for geometry optimization and electronic property calculations. Total energy changes are reduced to $< 1 \times 10^{-4}$ eV per atom, and structures are relaxed until all residual forces are < 0.03 eV/Å. For all calculations, spin polarization is considered.

The formation energy of the defect X in charge state q is defined as [32]

$$E_f(X^q) = E_{tot}(X^q) - E_{tot}(bulk) - \Sigma_i n_i \mu_i$$
$$+ q[E_F + E_v + \Delta V_{0/b}] + E_{Corr}. \quad (1)$$

In the formula, at first, q is the total charge of the defect; $E_{tot}(X^q)$ is the total energy of the Bi_2MoO_6 with the X defect charge state of q in the supercell; $E_{tot}(bulk)$ is the total energy of the pristine Bi_2MoO_6 supercell; μ_i is the chemical potential of chemical species $i(i = Bi, Mo, O)$; n_i denotes the number of atoms of species i with chemical potential μ_i, which have been added to $(n_i > 0)$ or removed from $(n_i < 0)$ the supercell when forming the defect; and E_F is the Fermi level referenced to the VB maximum (VBM) in pure Bi_2MoO_6, varying between 0 and the band gap E_g. In this paper, $E_g = 2.635 (2.183)$ eV resulting from the HSE (PBE) calculations, E_v is the supercell energy difference between the pure host $(q = 0)$ and the host with one hole $(q = +1)$ in the VB in the dilute hole gas limit [33], and $\Delta V_{0/b}$ is another correction for the average electrostatic potential alignment of 1s core energy level of O atoms between the supercells with and without a defect [34].

Regarding charge-image interaction, the total energies of charged defects are inaccurate under a finite cell size, conflicting with the periodical boundary conditions used in DFT calculations [33,35,36]. Given by Lany and Zunger [32,33], the image-charge correction term E_{Corr} to account for supercell errors is written as

$$E_{corr} = [1 + f] \frac{q^2 \alpha}{2\varepsilon L}, \quad (2)$$

where q is the total charge of a defect defined as before, f is a shape factor related to the supercell geometries [32], α is the Madelung constant, and ε is the static dielectric constant of the pristine bulk. In this paper, the average static dielectric constant in three lattice directions is 34.59, calculated by density functional perturbation theory, which agrees with the experimental value of 31 [37,38], and L is the linear dimension of the supercell ($L = V^{1/3}$, V is the volume of the supercell).

The charge-state transition levels between q_1 and q_2 of point defects can be derived from the calculated formation energies, which can also be defined as [39–41]

$$\varepsilon\left(\frac{q_1}{q_2}\right) = \frac{E_f(X^{q_1}) - E_f(X^{q_2})}{q_2 - q_1}. \tag{3}$$

From Eq. (1), we can see $\varepsilon(q_1/q_2)$ corresponds to the Fermi level at which the formation energy of defects in charged state q_1 is equal to that in charged state q_2.

In the synthesis process, the chemical potentials of Bi, Mo, and O in Bi_2MoO_6 are not arbitrary but subject to thermodynamic constraints, which can be used to represent actual experimental conditions. Under thermal equilibrium growth conditions, it should be satisfied with the following equation for pure Bi_2MoO_6:

$$2\mu_{Bi} + \mu_{Mo} + 6\mu_O = \mu_{Bi_2MoO_4}, \tag{4}$$

where μ_{Bi}, μ_{Mo}, and μ_O represent the chemical potentials of Bi, Mo, and O atoms, respectively; and $\mu_{Bi_2MoO_4}$ is the chemical potential of Bi_2MoO_6. The total energy of the Bi_2MoO_6 ($E_{Bi_2MoO_4}$) per formula unit could be expressed as

$$E_{Bi_2MoO_4} = 2E_{Bi} + E_{Mo} + 6E_O + \Delta H_f(Bi_2MoO_6), \tag{5}$$

where $\Delta H_f(Bi_2MoO_6)$ is the formation enthalpy of Bi_2MoO_6, E_{Bi} is a reference to the energy of a Bi atom in trigonal Bi metal, E_{Mo} refers to the energy of a Mo atom in cubic Mo metal, and E_O is a reference to half of the total energy of an isolated O_2 molecule.

Under thermal equilibrium growth, $\mu_{Bi_2MoO_4} = E_{Bi_2MoO_4}$. That is,

$$2E_{Bi} + E_{Mo} + 6E_O + \Delta H_f(Bi_2MoO_6) = 2\mu_{Bi} + \mu_{Mo} + 6\mu_O. \tag{6}$$

Thus,

$$\begin{aligned}\Delta H_f&(Bi_2MoO_6) \\ &= 2(\mu_{Bi} - E_{Bi}) + (\mu_{Mo} - E_{Mo}) + 6(\mu_O - E_O) \\ &= 2\Delta\mu_{Bi} + \Delta\mu_V + 6\Delta\mu_O, \end{aligned} \tag{7}$$

where $\Delta\mu_{Bi} = (\mu_{Bi} - E_{Bi})$, $\Delta\mu_{Mo} = (\mu_{Mo} - E_{Mo})$, and $\Delta\mu_O = (\mu_O - E_O)$ are defined as the changes of the chemical potentials from their corresponding elemental phase (bulk/gaseous) to the compound phase, respectively, depending on the growth environment.

To prevent the formation of bulk Bi and Mo as well as loss of O_2, the restrictions of the chemical potentials should be

$$\Delta\mu_{Bi} < 0, \quad \Delta\mu_{Mo} < 0, \quad \Delta\mu_O < 0. \tag{8}$$

TABLE I. Calculated energy of formation per formula unit of Bi_2MoO_6 and the possible competing phases by PBE and HSE calculations. Experimental values are provided for comparison (unit: eV).

	PBE	HSE	Experiment
$\Delta H_f(Bi_2MoO_6)$	−15.04	−14.60	−16.83 [27]
$\Delta H_f(MoO_2)$	−5.91	−5.86	−6.465 [42]
$\Delta H_f(MoO_3)$	−7.84	−7.73	−8.876 [43]
$\Delta H_f(Bi_2O_3)$	−6.20	−5.87	−7.37 [44]

Moreover, to avoid the formation of the dual competing phases during the growth processing of Bi_2MoO_6, it is also required that

$$\Delta\mu_{Mo} + 2\Delta\mu_O < \Delta H_f(MoO_2), \tag{9}$$

$$\Delta\mu_{Mo} + 3\Delta\mu_O < \Delta H_f(MoO_3), \tag{10}$$

$$2\Delta\mu_{Bi} + 3\Delta\mu_O < \Delta H_f(Bi_2O_3). \tag{11}$$

For each formula unit, the PBE and HSE calculated formation energy of MoO_2, MoO_3, Bi_2O_3, and Bi_2MoO_6 are shown in Table I compared with the available experimental values. It is found that the results of PBE and HSE calculations are basically the same for formation energy and in excellent agreement with the experimental ones. The experimental crystal constants in Table II are used, starting for all the PBE and HSE calculations.

Equations (4)–(8) define the chemical potential in the tetrahedron with three vertices determined by $\Delta\mu_{Mo}$, $\Delta\mu_{Bi}$, and $\Delta\mu_O$, and the origin of coordinates indicates that Mo, Bi, and O are all rich. Vertex X_{HSE} ($\Delta\mu_{Bi}$, $\Delta\mu_{Mo}$, $\Delta\mu_O$) = (−7.30, 0, 0) eV means Mo/O is rich and Bi is poor. Vertex Y_{HSE} ($\Delta\mu_{Bi}$, $\Delta\mu_{Mo}$, $\Delta\mu_O$) = (0, −14.60, 0) eV means Bi/O is rich and Mo is poor. Vertex Z_{HSE} ($\Delta\mu_{Bi}$, $\Delta\mu_{Mo}$, $\Delta\mu_O$) = (0, 0, −2.43)eV means Mo/Bi is rich and O is poor. For the sake of intuition, the tetrahedron is projected on the $\Delta\mu_{Mo}$, $\Delta\mu_{Bi}$ two-dimensional plane, and the projection is a triangle, shown in Fig. 1 for HSE calculations. In the triangle, the origin (0, 0) means that both Bi and Mo are rich; $\Delta\mu_O = \Delta H_f(Bi_2MoO_6)/6 = -2.43$ eV; that is, O is poor. Point X_{HSE} (−7.30, 0) means Bi is poor, and Mo/O is rich. Point Y_{HSE} (0, −14.60) means Mo is poor and O/Bi is rich. The point on the hypotenuse $X_{HSE}Y_{HSE}$ means $\Delta\mu_O = 0$; in other words, O is rich. Each line segment parallel to the hypotenuse represents that $\Delta\mu_O$ is equal to a constant, which keeps decreasing from the hypotenuse of the triangle to the origin. We consider some representative points with coordinates ($\Delta\mu_{Bi}$, $\Delta\mu_{Mo}$, $\Delta\mu_O$) in units of eV, A_{HSE} (−3.44, −7.73, 0), G_{HSE} (−0.63, −2.11, −1.87), D_{HSE} (0, −1.48, −2.19), F_{HSE} (0, −2.86, −1.96), E_{HSE} (−2.94, −8.73, 0), marked on Fig. 1. A similar result by PBE functional is shown in the Supplemental Material (Fig. S1) [48]. Comparing Figs. 1 and S1 in the Supplemental Material [48], we find that the PBE and HSE results have almost the same stable regions for Bi_2MoO_6. Our PBE results are consistent with the previous theoretical research performed by Jing *et al.* [19].

TABLE II. Experimental lattice constants are provided for comparison with the PBE and HSE energy calculations. The lattice values of a, b, and c of each material are in Å.

	k-points	Space group	Experimental lattice constants
Mo	$10 \times 10 \times 10$	$Im-3m$	$a = b = c = 3.16; \alpha = \beta = \gamma = 90°$ [45]
MoO$_2$	$6 \times 6 \times 6$	$P21/c$	$a = 5.61, b = 4.86, c = 5.63;$ $\alpha = \gamma = 120.95°, \beta = 90°$ [46]
MoO$_3$	$2 \times 9 \times 8$	$Pnma$	$a = 13.86, b = 3.70, c = 3.96;$ $\alpha = \beta = \gamma = 90°$ [47]
Bi$_2$O$_3$	$7 \times 3 \times 4$	$P21/c$	$a = 5.85, b = 8.16, c = 11.17;$ $\alpha = \gamma = 120.95°, \beta = 90°$ [44]

III. RESULTS AND DISCUSSION

A. Formation energy of intrinsic defects

We have explored eight intrinsic point defects in the Bi$_2$MoO$_6$ lattice: V_{Bi} (Bi vacancy), V_{Mo} (Mo vacancy), V_O (O vacancy), I_{Bi} (interstitial Bi), I_{Mo} (interstitial Mo), I_O (interstitial O), Bi$_{Mo}$ (Bi replacing Mo), and Mo$_{Bi}$ (Mo replacing Bi). The formation energies of charge states for each defect as a function of the Fermi level referenced to VBM are shown in Fig. 2 for the HSE functional under different chemical potentials (see Supplemental Material [48], Fig. S2 for PBE). From the conventional point of view, without considering the thermal activations of impurity level and band edge, the Fermi level is pinned at the intersection of the formation energy
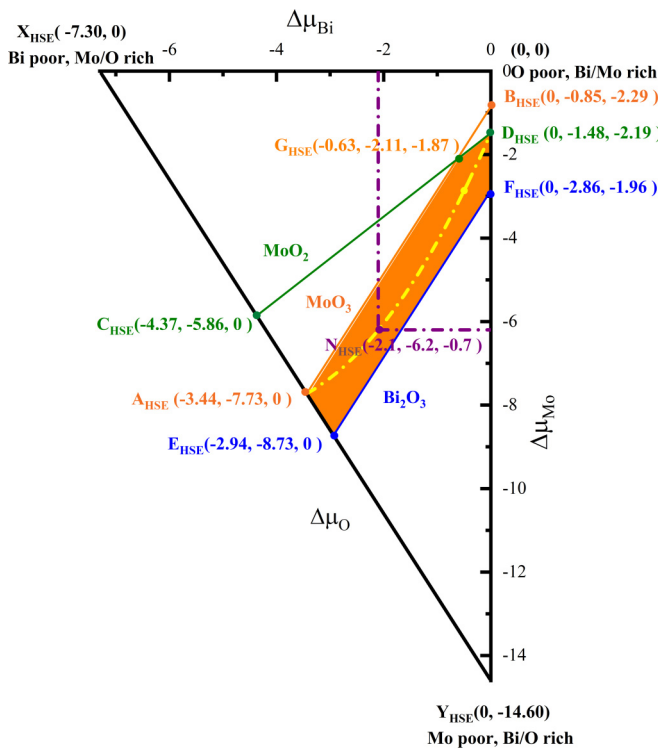

FIG. 1. The accessible range of chemical potentials (orange region, unit: eV) for equilibrium growth conditions of Bi$_2$MoO$_6$ calculated by HSE functional. The points A$_{HSE}$, D$_{HSE}$, E$_{HSE}$, F$_{HSE}$, N$_{HSE}$, and G$_{HSE}$, as well as the dash-dotted line along A$_{HSE}$N$_{HSE}$D$_{HSE}$, are chosen as the representative chemical potentials for the following calculations. The vertical and horizontal purple dash-dotted lines are used to determine the moderate point N$_{HSE}$.

lines of the lowest acceptor and donor [49,50]. Our results are shown by the red dashed line in Fig. 2. It is noted that, if the pinned Fermi level is above midgap, the material exhibits n-type conductivity. The closer the pinned Fermi level is to the conduction band minimum (CBM), the higher the electron density is [49]. In Fig. 2, for all the chemical conditions (A$_{HSE}$, D$_{HSE}$, E$_{HSE}$, F$_{HSE}$, N$_{HSE}$, and G$_{HSE}$), the Fermi level is pinned within the n-type region, which agrees with the experimental results [51]. So do the results of PBE (see Supplemental Material [48], Fig. S2) calculations except for E-point chemical conditions. Under E-point conditions, the Fermi level pinning in the p-type region has never been reported by the present experiments, partly showing the unreliability of the PBE method in the Bi$_2$MoO$_6$ system.

At the O-rich point A$_{HSE}$, the lowest-energy defect is Mo$_{Bi}^{3+}$ for $E_F < 1.5$ eV and V_{Bi}^{3-} for $E_F > 1.8$ eV, with V_O^{2+} having the lowest energy for E_F between these ranges. When thermal excitation is not considered, the Fermi level is pinned by V_{Bi}^{3-} and V_O^{2+} to be at ~ 0.8 eV below the CBM. One would expect E_F to remain trapped roughly midgap, resulting in an intrinsically insulating material [52]. From A$_{HSE}$ to E$_{HSE}$, with $\Delta\mu_{Bi}$ increasing and $\Delta\mu_{Mo}$ decreasing, the formation energy of the antisite defect Bi$_{Mo}$ decreased, but that of Mo$_{Bi}$ and Bi$_{vac}$ increased, while that of V_O remained almost unchanged. Thus, the Fermi level is pinned most nearly at the midgap by Bi$_{Mo}^{1-}$ and V_O^{2+} with the lowest formation energies, indicating the occurrence of the most typical self-compensation. As a result, under O-rich conditions (A$_{HSE}$ and E$_{HSE}$), the Fermi pinning near midgap and self-compensation between donors and acceptors would limit its n-type conductivity [53]. This implied that such extreme O-rich growth conditions should be avoided.

At the Bi-rich point D$_{HSE}$, the Fermi level is pinned to be at ~ 0.3 eV below the CBM by the favorable acceptor V_{Bi}^{3-} and donor I_{Mo}^{3+}, showing typical n-type conductivity. Nevertheless, the donor defects Mo$_{Bi}$ and V_O had the lowest energy for $E_F > 1.5$ eV, showing that they are easier to form. With $\Delta\mu_O$ increasing and $\Delta\mu_{Mo}$ decreasing from D$_{HSE}$ to F$_{HSE}$, the formation energy of the antisite defect Bi$_{Mo}$ shifted downward, lower than that of V_{Bi}, while that of Mo$_{Bi}$ shifted upward. Thus, the Fermi level is pinned to be at ~ 0.1 eV below the CBM by the favorable acceptor Bi$_{Mo}^{3-}$ and donor Mo$_{Bi}^{2+}$, in which the Fermi pinning is closest to the CBM, making strong n-type conductivity and a higher electron concentration [49]. At the same time, the donor defect V_O has the lowest energy when the Fermi level is close to the CBM, suggesting its easy forming. Overall, our results implied that, to obtain excellent
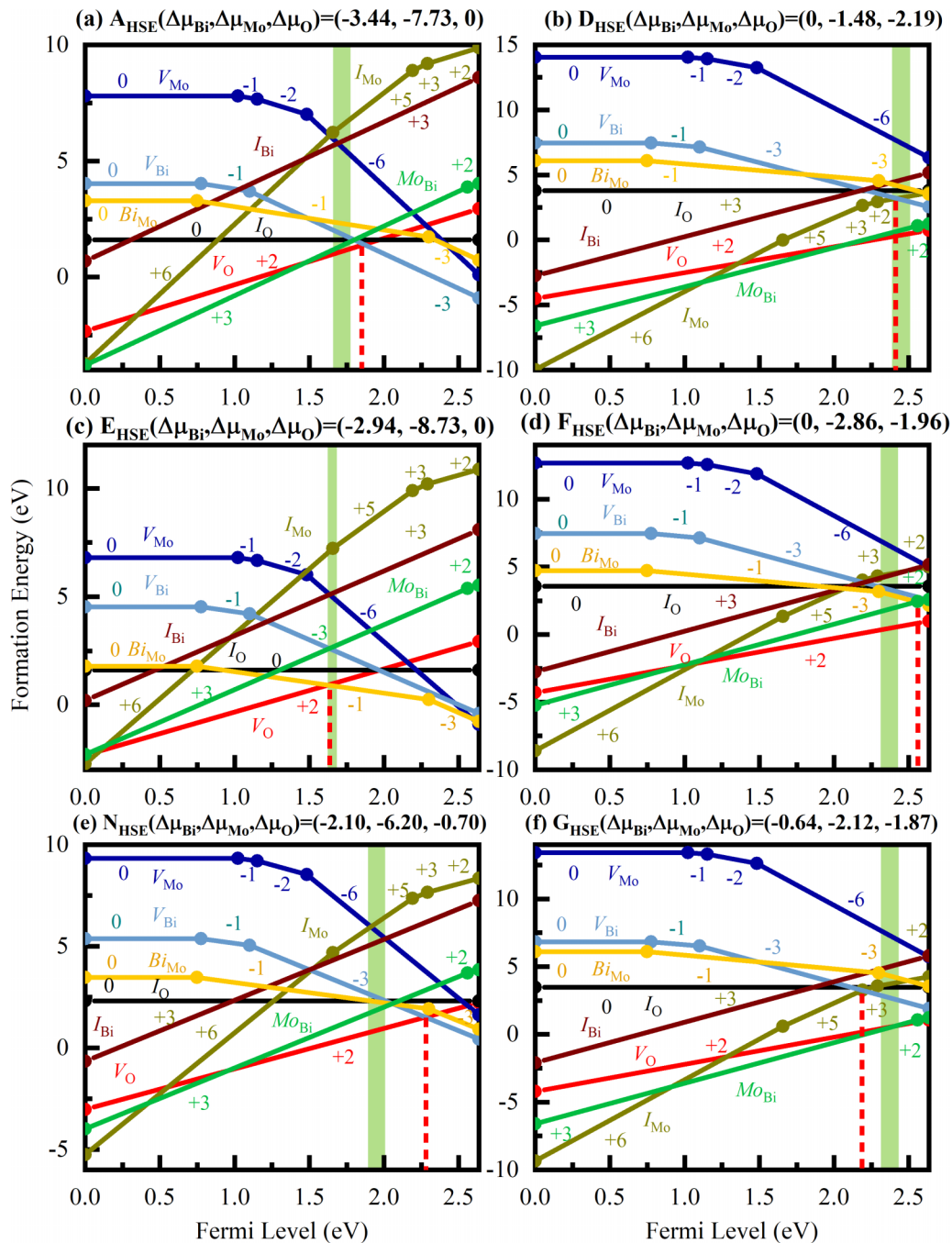
FIG. 2. The formation energies (derived from HSE calculation) of intrinsic defects in Bi_2MoO_6 plotted as a function of the Fermi level with respect to the valence band maximum (VBM) under A_{HSE}, D_{HSE}, E_{HSE}, F_{HSE}, N_{HSE}, and G_{HSE} chemical potential conditions. Each defect corresponds to a polygonal line formed only by the segments associated with the lowest-energy charge states, in which the kinks connecting different segments indicate the transition levels. The slope of each segment is denoted by the number on them, displaying the charge state. The different parallel line segments between different defects imply the same charge state. The Fermi-level pinning is indicated by red dash-dotted lines. The light green cylindrical zone (LGCZ) represents the ranges of the self-consistent Fermi levels as a function of temperature T from 20 to 900 K.

n-type conductivity, Bi_2MoO_6 should be synthesized under Bi-rich/O-poor conditions.

Moreover, at the moderate point N_{HSE}, the Fermi level is pinned by V_{Bi}^{3-} and V_O^{2+}. At point G_{HSE}, the Fermi level is pinned by V_{Bi}^{3-} and I_{Mo}^{3+}, but for $E_F > 1.5$ eV, the lowest-energy defects are V_O and Mo_{Bi}, indicating they are easier to form.

B. Self-consistent Fermi energy, equilibrium carrier and defect concentrations

1. The temperature effect

To more quantitatively investigate the defect properties under certain temperatures, we calculate the self-consistent Fermi level (E_F), equilibrium electron carrier concentrations
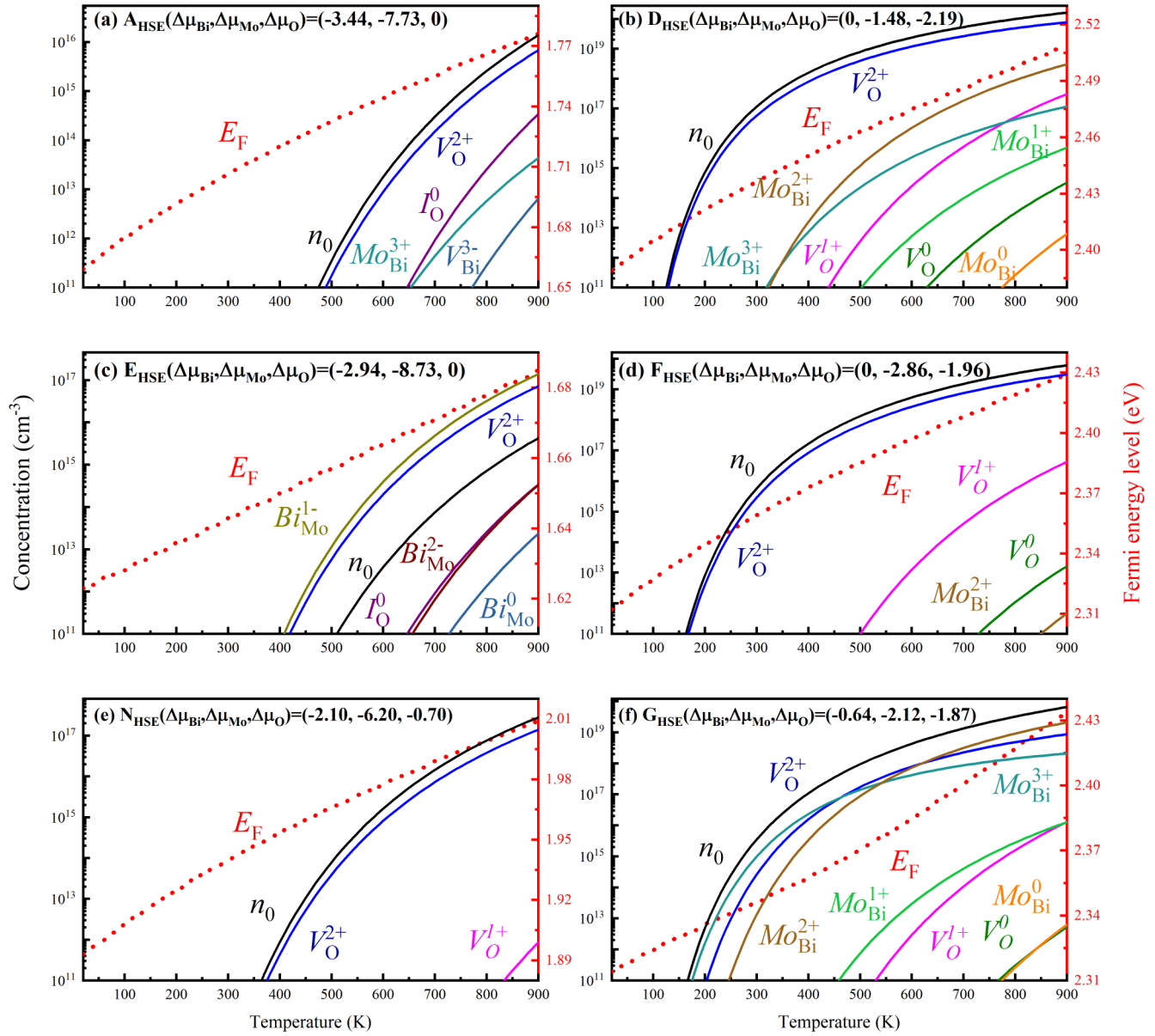
FIG. 3. The self-consistent Fermi energy (E_F, red dash-dotted line, right axis), n_0, and mainly each charged defect concentration (color solid lines, left axis) as a function of temperature from 20 to 900 K for the intrinsic defect in Bi$_2$MoO$_6$ under different chemical potential conditions of (a) A$_{HSE}$, (b) D$_{HSE}$, (c) E$_{HSE}$, (d) F$_{HSE}$, (e) N$_{HSE}$, and (f) G$_{HSE}$ derived from HSE calculations.

(n_0), and defect concentrations (denoted as $[X_{defect}^q]$) as a function of T under different chemical potential conditions with the dilute defect approximation in Bi$_2$MoO$_6$. The results are shown in Fig. 3 for each charged defect by HSE using the code SC-FERMI [52,54] under charge neutrality conditions (Supplemental Material [48], Note S1). Following Refs. [52,54] for simplification, we have assumed the defect formation energies, unit cell parameters, the total density of states, and band gap of pure Bi$_2$MoO$_6$ do not change with T.

As shown in Fig. 3, with the temperature from 20 to 900 K, E_F by HSE is 1.659–1.776 eV (A$_{HSE}$), 2.389–2.509 eV (D$_{HSE}$), 1.623–1.685 eV (E$_{HSE}$), 2.312–2.429 eV (F$_{HSE}$), 1.893–2.009 eV (N$_{HSE}$), and 2.314–2.434 eV (G$_{HSE}$), increasing with thermal excitation [50]. They have been added in Fig. 2 with a light green cylindrical zone (LGCZ), which

agrees with the previous study [52]. There is some discrepancy between the self-consistent E_F and the traditional Fermi level pinning (red dash-dotted lines in Fig. 2). It is derived from the thermal excitations (electrons/holes from CBM/VBM and defect energy level) at finite temperature [50]. It is well known that the Fermi energy position often varies with temperature as well as dopant concentration. We noted that, under the charge-neutral condition, considering the overall effect of all defects and thermal excitation at a specific temperature, E_F naturally has a more realistic prediction effect than the Fermi pinning. This is because most of the Fermi pinning only considers the lowest-energy donor and acceptor, which formation energy lines only intersect in the band gap. At the same time, only when there are no defects with lower energy than the two intersecting defects presenting can the

calculated E_F and the Fermi pinning be approximately coincident. Only then the Fermi pinning will play a leading role in the analysis of material conductivity, which will be seen in the following.

Meanwhile, as seen in Fig. 3, we found that the order of charged defect concentration from high to low is consistent with the order of defect formation energy from low to high in the LGCZ (Fig. 2) instead of the whole band gap from VBM to CBM, according to Eq. (1) and the Supplemental Material [48], Eqs. (S3) and (S4). The defect with the lowest formation energy in the LGCZ has the highest concentration. Thus, the influence of E_F on formation energy and even concentration of defects is more complex than the linear relationship in Eq. (1) after considering the temperature effect [50]. Using the specific positions of Fermi energy levels in the formation energy vs Fermi level diagram (Fig. 2), which is determined by temperature, doping concentration, chemical potentials, and so on, one can infer the concentration relationship of these intrinsic defects.

Under O-rich conditions, at point A_{HSE}, as shown in Fig. 3(a), E_F is close to midgap. Here, n_0 (equal to $2[V_O^{2+}]$) is lower than 10^{16} cm^{-3}, mainly from the secondary ionization of V_O. The highest concentration of V_O^{2+} is derived from its lowest formation energy in the LGCZ of the E_F [Fig. 2(a)]. At point E_{HSE} [Fig. 3(c)], the typical self-compensation between Bi_{Mo}^{1-} and V_O^{2+} takes place, so $[Bi_{Mo}^{1-}] = 2[V_O^{2+}]$ always holds, resulting in the lower carrier density ($n_0 < 10^{15}$ cm^{-3}) with E_F close to midgap. Obviously, n_0 is too low ($< 10^{17}$ cm^{-3}) to be used for successful photocatalytic materials under O-rich growth conditions [55]. This suggests that O-rich growth conditions should be avoided or further modified, which agrees with our previous analysis of formation energy vs Fermi level [Figs. 2(a) and 2(c)].

Under Bi-rich conditions (D_{HSE} and F_{HSE} in Fig. 3), as E_F is closer to the CBM, Bi_2MoO_6 behaves as a strong n-type with $n_0 > 10^{19}$ cm^{-3} at $T \sim 700$ K. The source of n_0 comes from the secondary ionization of V_O, so $n_0 = 2[V_O^{2+}]$ holds. The dominant defect V_O^{2+} has the highest concentration with the lowest formation energy in the LGCZ [Figs. 2(b) and 2(d)], which is compensated by n_0 (to maintain charge neutrality) with no significant intrinsic compensation. Therefore, V_O^{2+} is the dominant defect. However, this defect might act either as an active defect site to enhance the photocatalytic activity further or as a recombination center for electron-hole pairs to harm its photocatalytic properties (see Supplemental Material [48], Note S2). To address these issues, we calculated the spin-polarized density of the states (DOS) for V_O^{2+} by HSE (see Supplemental Material [48], Fig. S3(d)). Our results show no impurity energy band in the gap region without the recombination center of electrons and holes, which is consistent with the previous PBE functional calculations [19]. Moreover, the band gap of V_O^{2+} is decreased, improving its capacity for light absorption. With the increase of T, the increasing n_0 leadd to improved photocatalytic properties, which can be used to explain that the photocatalytic efficiency for tetracycline by Bi_2MoO_6 calcined at $450°$ C is 17% higher than that of pristine Bi_2MoO_6 after 150 min light irradiation [17]. As shown in the LGCZ of E_F in Figs. 2(b) and 2(d), the formation energies of Mo_{Bi}^{3+}, Mo_{Bi}^{2+}, and V_O^{1+} (not shown) are ~ 0.02 eV in Fig. 2(b) and ~ 0.15 eV in Fig. 2(d) higher than that of V_O^{2+},

respectively. However, $[Mo_{Bi}^{3+}]$, $[Mo_{Bi}^{2+}]$, and $[V_O^{1+}]$ are at least one order of magnitude in Fig. 3(b) and 3-7 orders of magnitude in Fig. 3(d) smaller than $[V_O^{2+}]$, respectively, which have often been omitted. The reason is the exponential relationship between defect concentration and its formation energy (Supplemental Material [48], Eq. (S3)). Therefore, the higher carrier concentration and excellent electronic properties of Bi_2MoO_6 can be obtained under Bi-rich/O-poor conditions.

At the moderate point N_{HSE} [Fig. 3(e)], $2[V_O^{2+}] = n_0$ always holds without the obvious appearance of other intrinsic defects, but n_0 is $< 10^{17}$ cm^{-3}. At G_{HSE}, the most favorable charged defects are Mo_{Bi}^{2+}, Mo_{Bi}^{3+}, and V_O^{2+} shown in Fig. 3(f) almost having similar formation energies in the LGCZ of Fig. 2(f). The charge neutrality condition of $2[Mo_{Bi}^{2+}] + 3[Mo_{Bi}^{3+}] + 2[V_O^{2+}] = n_0$ always holds, indicating that the donors of Mo_{Bi}^{2+}, Mo_{Bi}^{3+}, and V_O^{2+} coexist in equal order of magnitude and are compensated predominantly by electron carriers $> 10^{19}$ cm^{-3} with strong n-type conductivity. The electronic properties of Mo_{Bi}^{3+} are as good as that of V_O^{2+} (shown in the Supplemental Material [48], Fig. S3(j) by HSE). However, the DOS of Mo_{Bi}^{2+} has an occupied deep level in the gap at ~ 1.2 eV above the VBM, shown in the Supplemental Material [48], Fig. S3(i) by HSE. This deep defect level can act as a recombination center of holes and electrons, which harms its photocatalytic properties. Correspondingly, as shown in the Supplemental Material [48], Fig. S4(e), the wave function of Mo_{Bi}^{2+} is only distributed around the Mo atom substituting for Bi, showing a localized feature. Therefore, although n_0 is higher ($> 10^{19}$ cm^{-3}) at the G_{HSE} point, the Mo_{Bi}^{2+} defects can serve as recombination centers of holes and electrons with large concentrations; thus, the photocatalytic performance of Bi_2MoO_6 cannot be well improved.

2. The chemical potentials along A_{HSE} E_{HSE}

To further comprehensively understand the detailed changes of intrinsic defect concentration and compensation relationship with chemical potentials, E_F, n_0, and the dominant defects concentration with mainly charged states as a function of chemical potentials along A_{HSE} E_{HSE} and $A_{HSE}N_{HSE}$ D_{HSE} (Fig. 1) at a given thermodynamic equilibrium temperature and after quenching are investigated. We set the solid-state synthesized temperature of 700 K [56,57] of Bi_2MoO_6 as the growth temperature, and then it is quenched to a working temperature (300 K). We assume that the total concentration of each intrinsic defect is unchanged over all possible valences generated at high temperatures. In contrast, each charged state concentration is redistributed according to its new weight after the rapid quenching [58,59] following the procedure FROZEN-SC-FERMI [54] (Supplemental Material [48], Note S1). With the help of this code, we can also approximately analyze how the balance of intrinsic defect concentration is affected by extrinsic charged defects of fixed concentration without knowing the formation energy of extrinsic charged defects [52,54]. In this paper, the concentration of the extrinsic defects is fixed at 10^{18} cm^{-3}, as adopted by Refs. [52,54,60]. In general, donor doping is expected to introduce electrons in the system, which can effectively increase the electrical conductivity and improve the photocatalytic performance.
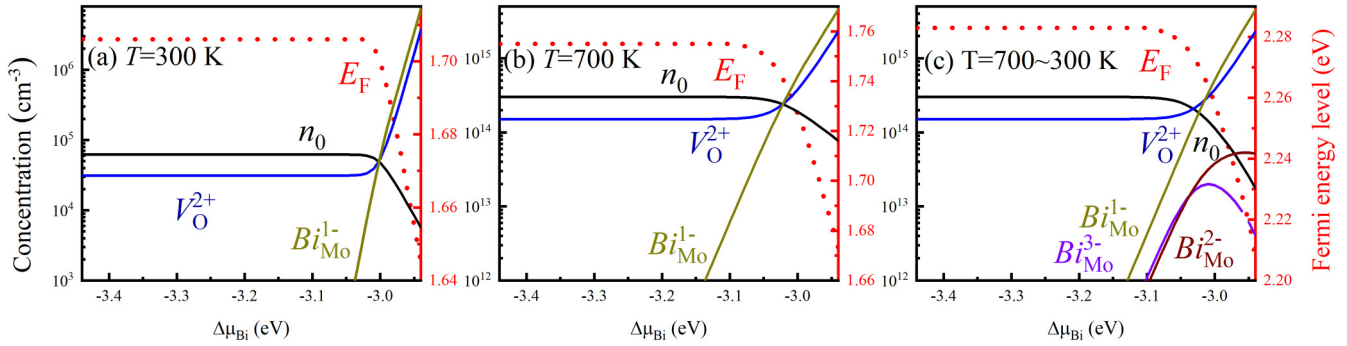
FIG. 4. The self-consistent Fermi energy (E_F, red dash-dotted line, right axis), n_0, and the mainly intrinsic defect concentration (solid color line, left axis) calculated by HSE as a function of $\Delta\mu_{Bi}$ for only intrinsic defects in Bi_2MoO_6 under thermodynamic equilibrium conditions (a) at 300 K, (b) at 700 K, and (c) under nonthermodynamic equilibrium conditions quenched from 700 to 300 K, along the straight line $A_{HSE}E_{HSE}$ (Fig. 1).

Firstly, as shown in Fig. 4, E_F, n_0, and main defect concentration as a function of $\Delta\mu_{Bi}$ (coequally in the Supplemental Material [48], Fig. S5 of $\Delta\mu_{Mo}$) are calculated under O-rich conditions (along A_{HSE} E_{HSE}, $\Delta\mu_O = 0$). This is because most experiments are performed in air atmosphere [61–63]. At $T = 300$ K, when $\Delta\mu_{Bi} < -3.05$ eV, as shown in Fig. 4(a), (corresponding to $\Delta\mu_{Mo} > -8.05$ eV, Supplemental Material [48], Fig. S5(a)), the charge neutrality condition is satisfied by $2[V_O^{2+}] = n_0$. This suggests that there is no significant intrinsic defect compensation. Here, $[V_O^{2+}]$ and n_0 remain unchanged in this range because their Fermi levels remain basically fixed and almost cancel exactly the change of the chemical potentials [50], showing that attempts to regulate defect formation by adjusting chemical potential will fail in this range [50]. For $\Delta\mu_{Bi} > -3.05$ eV in Fig. 4(b) (for $\Delta\mu_{Mo} < -8.05$ eV in the Supplemental Material [48], Fig. S5(b)), $[Bi_{Mo}^{1-}]$ begins increasing rapidly and becomes closer to $[V_O^{2+}]$; after that, $[Bi_{Mo}^{1-}]$ and $[V_O^{2+}]$ increase sharply together and compensate for each other. The typical self-compensation makes the E_F drop rapidly, which can also be seen at E_{HSE} in Fig. 3(c). Thus, n_0 drops seriously, leading to reduced conductivity. On the other hand, at 700 K [Fig. 4(b)] and after quenching [Fig. 4(c)], the trends of the Fermi energy level and carrier and defect concentrations are basically

consistent with those at 300 K, except for numerical enhancement. When the temperature is from 300 to 700 K (Fig. 4), n_0 and $[V_O^{2+}]$ increase by ~10 orders of magnitude, and the Fermi energy level moves toward the CBM since the defect thermal excitation intensifies at a higher temperature. When the system is rapidly quenched to room temperature, the thermal activation of the dominant V_O^{2+} is kept strong, while the band-edge thermal excitation is largely suppressed to decrease the hole concentration, resulting in a shift of the Fermi level toward the CBM again [50,59]. After quenching, for $\Delta\mu_{Bi} < -3.05$ eV, n_0 and $[V_O^{2+}]$ can be enhanced from 10^4 cm^{-3} at 300 K to 10^{14} cm^{-3} at 700 K, still showing its low conductivity only with the intrinsic defect states under O-rich conditions. To improve its carriers concentration, dopant doping was a well-known method to adopt in semiconductor research.

Secondly, when acceptors ($[A^-] = 10^{18}$ cm^{-3}) are doping into Bi_2MoO_6 along $A_{HSE}E_{HSE}$, as shown in the Supplemental Material [48], Fig. S6 for $\Delta\mu_{Bi}$ (Fig. S7 for $\Delta\mu_{Mo}$), n_0 is almost equal to 0 at $T = 300$ K (see Supplemental Material [48], Fig. S6(a)) and is always $< 10^{13}$ cm^{-3} at 700 K (see Supplemental Material [48], Fig. S6(b)) and even after quenching from 700 to 300 K (see Supplemental Material [48], Fig. S6(c)), due to A^- mainly compensated by V_O^{2+}. It shows that
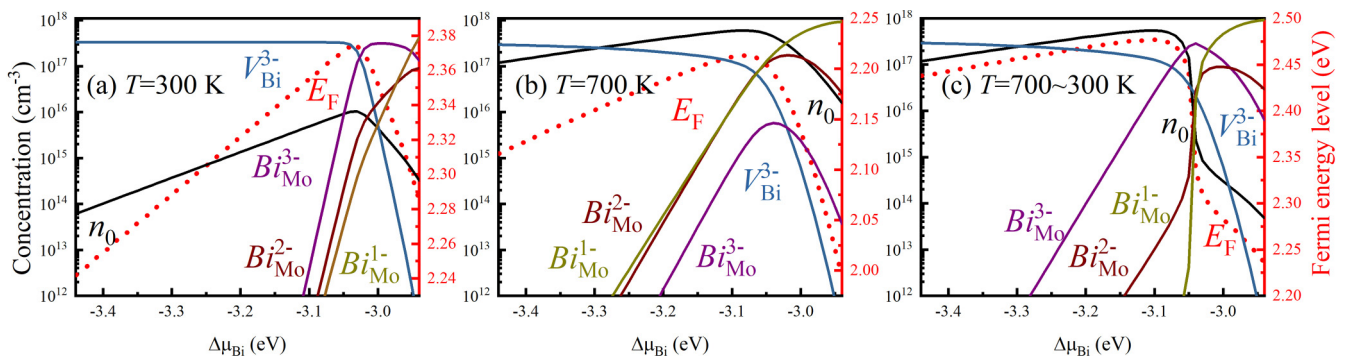

FIG. 5. The self-consistent Fermi energy (E_F, red dash-dotted line, right axis), n_0, the mainly intrinsic defect concentration (solid color line, left axis) by HSE as a function of $\Delta\mu_{Bi}$ under thermodynamic equilibrium condition (a) at 300 K, (b) at 700 K, and (c) under nonthermodynamic equilibrium conditions quenched from 700 to 300 K, in the presence of a fixed concentration of donors $[D^+] = 10^{18}$ cm^{-3} under O-rich conditions (along $A_{HSE}E_{HSE}$ in Fig. 1).
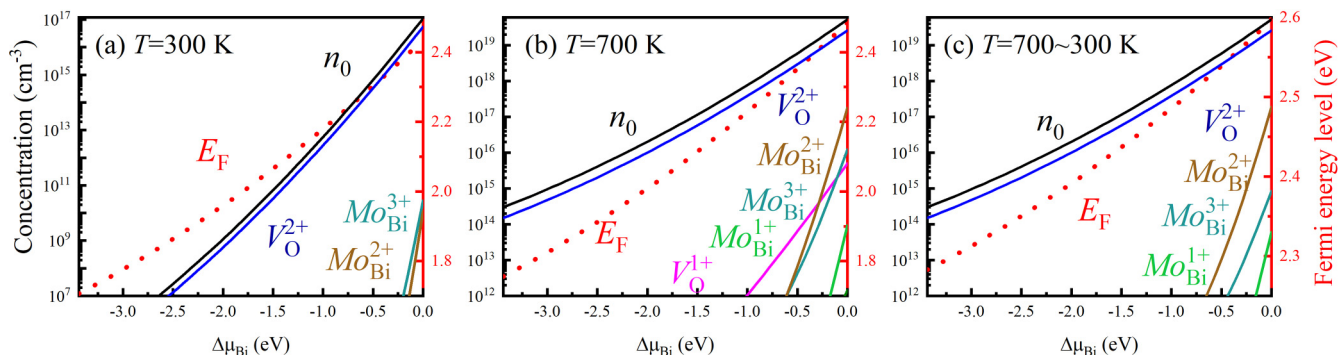
FIG. 6. The self-consistent Fermi energy (E_F, red dash-dotted line, right axis), n_0, and the mainly intrinsic defect concentration (solid color line, left axis) calculated by HSE as a function of $\Delta\mu_{Bi}$ for only intrinsic defects in Bi_2MoO_6 under thermodynamic equilibrium conditions (a) at 300 K, (b) at 700 K, and (c) under nonthermodynamic equilibrium conditions quenched from 700 to 300 K, along the curve $A_{HSE}N_{HSE}D_{HSE}$ (Fig. 1).

A^- doping will further inhibit the electron concentration of the intrinsic *n*-type Bi_2MoO_6 under O-rich conditions. Therefore, different attempts should be made to obtain a higher carrier density.

Thirdly, when donors ($[D^+] = 10^{18}$ cm^{-3}) are doping into Bi_2MoO_6 along A_{HSE} E_{HSE} (Fig. 5), E_F gradually rises to its maximum for $\Delta\mu_{Bi} < -3.05$ eV. After that, E_F drops quickly under both thermodynamic and nonthermodynamic equilibrium conditions. Accordingly, n_0 rises to the maximum value and then begins to decline, which can even be $>10^{17}$ cm^{-3} at 700 K and after quenching. Additionally, for $\Delta\mu_{Bi} < -3.05$ eV, compared with 300 K, the compensation effect of intrinsic acceptor V_{Bi}^{3-} on D^+ is weakened at 700 K and after quenching, resulting in a significant increase of n_0. For $\Delta\mu_{Bi} > -3.05$ eV, Bi_{Mo} compensated for D^+ since E_F crosses the transition energy level $\varepsilon(3-/-)$ of Bi_{Mo} at 300 K and after quenching (in Fig. 2), which changes the dominant charge state of Bi_{Mo} from 3− to 1−. Surprisingly, with no value of E_F being the ground state in Fig. 2, Bi_{Mo}^{2-} at a certain amount also appears across the point of $\varepsilon(3-/-)$, adding the vital knowledge about the 2− state missing in Fig. 2 of formation energy vs Fermi level [54].

At 700 K, D^+ is compensated strongly by the intrinsic acceptors along the whole range of A_{HSE} E_{HSE}; the band-edge thermal excitation becomes dominant. It enhances the hole concentration in Bi_2MoO_6, which pushes the Fermi level closer to the VBM by ~0.15 eV than that at 300 K. After quenching, the thermally excited holes are dramatically suppressed. At the same time, the defect activation remains to further increase n_0 and to shift the Fermi level toward the CBM ~0.25 eV.

From the above analysis, we find that V_{Bi}^{3-} is the most important defect when D^+ doping. Thus, we calculate the electronic properties of V_{Bi}^{3-}, as shown in the Supplemental Material [48], Fig. S3(b) by HSE. There is no recombination center of electrons and holes in the gap region to be of harm to its photocatalytic performance, which is as good as those of V_O^{2+}.

For $-3.44 < \Delta\mu_{Bi} < -3.05$ eV in Fig. 5(c) ($-8.05 < \Delta\mu_{Mo} < -7.73$ eV in the Supplemental Material [48], Fig. S8(c)), we can obtain n_0 and $[V_{Bi}^{3-}]$ as $>10^{17}$ cm^{-3} with both the D^+ doping and quenching strategy in the air environment. These calculated electron concentrations are higher by >2 orders of magnitude than those for only intrinsic defects without D^+ doping [Fig. 4(c)]. Therefore, the problem of insufficient electron carrier concentration synthesized under air conditions can be solved and improved, which makes it possible to use Bi_2MoO_6 as a better photocatalytic material. Combined with
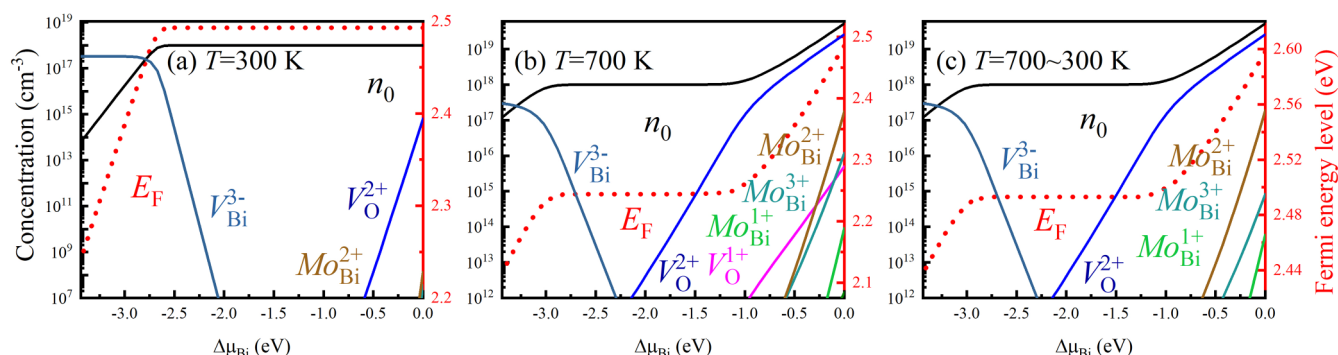

FIG. 7. The self-consistent Fermi energy (E_F, red dash-dotted line, right axis), n_0, the mainly intrinsic defect concentration (solid color line, left axis) by HSE as a function of $\Delta\mu_{Bi}$ under thermodynamic equilibrium condition (a) at 300 K, (b) at 700 K, and (c) under nonthermodynamic equilibrium conditions quenched from 700 to 300 K, in the presence of a fixed concentration of donors $[D^+] = 10^{18}$ cm^{-3} under O-rich conditions (along the curve $A_{HSE}N_{HSE}D_{HSE}$ in Fig. 1).

experimental results [12,15,64] of having improved the photocatalytic performance of Bi_2MoO_6 with oxygen vacancies under air conditions, we cannot help doubting whether it is by intentional or unintentional donor doping that good conductivity is achieved under O-rich conditions.

In addition, comparing Figs. 4, 5, and S5–S8 in the Supplemental Material [48], it can be seen clearly that the Fermi energy level changes not only with the chemical potential but also with the doping concentration, temperature, and other environmental factors.

3. The chemical potentials along $A_{HSE}N_{HSE}D_{HSE}$

To be more general, we calculate E_F, n_0, and defect concentrations as a function of $\Delta\mu_{Bi}$, shown in Fig. 6 along the $A_{HSE}N_{HSE}D_{HSE}$ curve (the chemical potentials from O-rich, Bi/Mo-poor to O-poor, Bi/Mo-rich conditions in Fig. 1; coequally in the Supplemental Material [48], Fig. S9 of $\Delta\mu_{Mo}$ and Fig. S10 of $\Delta\mu_O$) at $T = 300$ and 700 K and after quenching. It can be seen that E_F increases monotonously with $\Delta\mu_{Bi}$ and moves to the CBM at high temperature for the dominant defect excitation to enhance n_0, then goes on moving to the CBM after quenching, as previously dicussed [59]. Accordingly, n_0 from the fully ionized V_O increases monotonously, and $n_0 = 2[V_O^{2+}]$ holds. Thus, V_O^{2+} with perfect electronic properties (see Supplemental Material [48], Fig. S3(d)) is always the dominant defect. It can be seen that, after quenching, n_0 is $>10^{18}$ cm^{-3} [Fig. 6(c)] for -0.92 eV $< \Delta\mu_{Bi} < 0$. However, once deviating from these ranges, n_0 and $[V_O^{2+}]$ will decrease rapidly. It indicates that n_0 and intrinsic defect concentrations still need further improvement. Moreover, the same trends of $\Delta\mu_O$ in the Supplemental Material [48], Fig. S10, are consistent with the results presented in figs. 3 and 4 of Ref. [65,66], in which n_0 decreased with the oxygen partial pressure or temperature increasing as usual [67,68].

After doping A^- into Bi_2MoO_6, the calculated E_F, n_0, and defect concentrations as a function of $\Delta\mu_{Bi}$ along $A_{HSE}N_{HSE}D_{HSE}$ are shown in the Supplemental Material [48], Fig. S11 (coequally in Fig. S12 of $\Delta\mu_{Mo}$ and Fig. S13 of $\Delta\mu_O$). At $T = 300$ K, n_0 remains quite low compared with the concentrations of V_O^{2+}. At $T = 700$ K (see Supplemental Material [48], Fig. S11(b)) and after quenching (see Supplemental Material [48], Fig. S11(c)), the trends of E_F and n_0 changing are alike in Fig. 6, where there are only intrinsic defects. Here, n_0 is $<10^{18}$ cm^{-3}, as A^- is mainly compensated by V_O^{2+} for -3.44 eV $< \Delta\mu_{Bi} < -1.00$ eV (see Supplemental Material [48], Fig. S11), -7.73 eV $< \Delta\mu_{Mo} < -4.00$ eV (see Supplemental Material [48], Fig. S12), and -1.50 eV $< \Delta\mu_O < 0$ (see Supplemental Material [48], Fig. S13), meaning that the acceptor doping is inefficient. Moreover, n_0 will become $>10^{18}$ cm^{-3} for -0.85 eV $< \Delta\mu_{Bi} < 0$ (see Supplemental Material [48], Fig. S11), -6.30 eV $< \Delta\mu_{Mo} < -1.48$ eV (see Supplemental Material [48], Fig. S12), and -2.19 eV $< \Delta\mu_O < -0.74$ eV (see Supplemental Material [48], Fig. S13) and will continue to rise with the chemical potential changing. The $[V_O^{2+}]$ increases above the value necessary to compensate $[A^-]$, while E_F is pushed closer to the CBM. However, n_0 is higher only in a small range of chemical potentials near Bi-rich conditions, indicating the difficulty to observe it

experimentally. As a result, doping with $[A^-]$ along the direction of $A_{HSE}N_{HSE}D_{HSE}$ displays a negative-regulation effect on the equilibrium electron carrier concentrations (n_0). Thus, other modulation studies are required.

After doping D^+ into Bi_2MoO_6, the calculated E_F, n_0, and defect concentrations as a function of $\Delta\mu_{Bi}$ along $A_{HSE}N_{HSE}D_{HSE}$ are shown in Fig. 7 (coequally in the Supplemental Material [48], Fig. S14 of $\Delta\mu_{Mo}$ and Fig. S15 of $\Delta\mu_O$). At $T = 300$ K, when $\Delta\mu_{Bi}$ changes from -3.44 to -2.50 eV [Fig. 7(a)], n_0 increases as E_F increases slightly. Here, D^+ is mainly compensated by V_{Bi}^{3-}, so $3[V_{Bi}^{3-}] = [D^+]$ holds. For $\Delta\mu_{Bi} > -2.50$ eV, $[V_{Bi}^{3-}]$ drops quickly, and E_F also keeps basically fixed and almost cancels exactly the change of the chemical potentials [50], where no significant defect compensation is observed, n_0 mainly contributes by D^+, and $n_0 = [D^+]$ keeps, the so-called *suppression region* of inherent defects by external donors.

At $T = 700$ K [Fig. 7(b)] and after quenching [Fig. 7(c)], E_F first rises with the increase of $\Delta\mu_{Bi}$ and then rises after a stable distance, in sharp contrast to the situation that E_F tends to be stable after rising at 300 K [Fig. 7(a)]. At 700 K, E_F slightly moves to the VBM due to the dominant band-edge thermal excitation to improve minority-carrier concentrations. After quenching, for the band edge excitation is strongly suppressed to heavily lower hole concentration by sharp cooling, and E_F significantly moves to the CBM, as previously mentioned [59]. For -3.44 eV $< \Delta\mu_{Bi} < -2.25$ eV, n_0 is $<10^{18}$ cm^{-3} due to the compensation between D^+ and V_{Bi}^{3-}. When $\Delta\mu_{Bi}$ changes from -2.25 to -1.27 eV, $[V_{Bi}^{3-}]$ drops quickly, and n_0 mainly contributes by D^+ as E_F remains unchanged, so $n_0 = [D^+] = 10^{18}$ cm^{-3}. This may imply that the influence of the intrinsic defects on D^+ doping is minimal. Thus, donor doping is efficient for Bi_2MoO_6 photocatalysts prepared in the experiment. For -1.27 eV $< \Delta\mu_{Bi} < 0$, n_0 is $>10^{18}$ cm^{-3} above $[D^+]$. As the chemical potential of Bi increases, $[V_O^{2+}]$ rises sharply, reaching $>10^{16}$ cm^{-3}, further contributing to the n-type activity. Under these conditions, n_0 is provided mainly by the secondary ionization of V_O.

On the whole, after quenching from 700 to 300 K, our results suggest that Bi_2MoO_6 will be easily donor doped under -2.50 eV $< \Delta\mu_{Bi} < 0$ [Fig. 7(c)], -6.32 eV $< \Delta\mu_{Mo} < -1.48$ eV (see Supplemental Material [48], Fig. S14(c)) and -2.19 eV $< \Delta\mu_O < -0.65$ eV (see Supplemental Material [48], Fig. S15(c)). These conditions are a broad range of chemical potentials, which shows that donor-doped Bi_2MoO_6 can be easily realized experimentally. Furthermore, under extreme O-poor and Bi/Mo-rich conditions after quenching, high n_0 can be obtained only by the easily forming of V_O^{2+} without consideration of D^- and A^+ doping.

IV. CONCLUSIONS

In summary, we have performed first-principles calculations to investigate the origin of n-type doping in Bi_2MoO_6 with intrinsic point defects. The self-consistent Fermi energies and equilibrium carrier and defect concentrations are calculated using the SC-FERMI code based on thermodynamic simulation. We found that the easy formation of V_O^{2+} is responsible for its intrinsic n-type conductivity under Bi-rich/O-poor conditions, and thus, it can have a very high

density (reaching up to 10^{19} cm^{-3}), making it the dominant defect in Bi$_2$MoO$_6$. Under more easily achieved experimental conditions, the calculated self-consistent Fermi energies and equilibrium carrier and defect concentrations show that n_0 is $>10^{17}$ cm^{-3} with the D$^+$ doping and quenching strategy. Moreover, under the broad range of chemical potentials, after quenching from 700 to 300 K, Bi$_2$MoO$_6$ can be effectively donor doped without significant compensation by intrinsic point defect formation, and n_0 increases as $\Delta\mu_O$ decreases or temperature increases. Therefore, the formation of compensating acceptor defects can be inhibited by choosing oxygen-poor (Bi-rich) growth conditions, and after quenching from 700 to 300 K. Our results provide guidelines for intrinsic defects doping in Bi$_2$MoO$_6$ and will

contribute to further improvement of the Bi$_2$MoO$_6$-based photocatalyst.

[1] M. Egashira, Phase diagram of the system Bi$_2$O$_3 \cdot$ MoO$_3$, J. Catal. **58**, 409 (1979).

[2] J. Bi, L. Wu, J. Li, Z. Li, X. Wang, and X. Fu, Simple solvothermal routes to synthesize nanocrystalline Bi$_2$MoO$_6$ photocatalysts with different morphologies, Acta Mater. **55**, 4699 (2007).

[3] X. Liu, S. Gu, Y. Zhao, G. Zhou, and W. Li, BiVO$_4$, Bi$_2$WO$_6$ and Bi$_2$MoO$_6$ photocatalysis: A brief review, J. Mater. Sci. Technol. **56**, 45 (2020).

[4] H. Yu, L. Jiang, H. Wang, B. Huang, X. Yuan, J. Huang, J. Zhang, and G. Zeng, Modulation of Bi$_2$MoO$_6$-based materials for photocatalytic water splitting and environmental application: A critical review, Small **15**, e1901008 (2019).

[5] Y. Ma, Y. Jia, L. Wang, M. Yang, Y. Bi, and Y. Qi, Exfoliated thin Bi$_2$MoO$_6$ nanosheets supported on WO$_3$ electrode for enhanced photoelectrochemical water splitting, Appl. Surf. Sci. **390**, 399 (2016).

[6] Q. Zhao, M. Long, H. Li, L. Wang, X. Bai, Y. Zhang, and D. Li, Synthesis of Bi$_2$MoO$_6$ and activating peroxymonosulfate to enhance photocatalytic activity under visible light irradiation, Cryst. Res. Technol. **56**, 2000219 (2021).

[7] J. Xu, Y. Liu, and M. Chen, Preparation of Cd-doped Bi$_2$MoO$_6$ photocatalyst for efficient degradation of ofloxacin under the irradiation of visible light, Surf. Interface **25**, 101246 (2021).

[8] Y. Zhong, Z. He, D. Chen, D. Hao, and W. Hao, Enhancement of photocatalytic activity of Bi$_2$MoO$_6$ by fluorine substitution, Appl. Surf. Sci. **467–468**, 740 (2019).

[9] L. Zhang, Z. Wang, C. Hu, and B. Shi, Enhanced photocatalytic performance by the synergy of Bi vacancies and Bi^0 in Bi^0 − Bi$_{2-\delta}$MoO$_6$, Appl. Catal. B **257**, 117785 (2019).

[10] L. Zhang, T. Xu, X. Zhao, and Y. Zhu, Controllable synthesis of Bi$_2$MoO$_6$ and effect of morphology and variation in local structure on photocatalytic activities, Appl. Catal. B **98**, 138 (2010).

[11] C. Huang, S. Ma, Y. Zong, J. Gu, J. Xue, and M. Wang, Microwave-assisted synthesis of 3D Bi$_2$MoO$_6$ microspheres with oxygen vacancies for enhanced visible-light photocatalytic activity, Photochem. Photobiol. Sci. **19**, 1697 (2020).

[12] X. Yang, S. Wang, N. Yang, W. Zhou, P. Wang, K. Jiang, S. Li, H. Song, X. Ding, H. Chen, and J. Ye, Oxygen vacancies induced special CO$_2$ adsorption modes on Bi$_2$MoO$_6$ for highly selective conversion to CH$_4$, Appl. Catal. B **259**, 118088 (2019).

[13] X. Ding, W. Ho, J. Shang, and L. Zhang, Self doping promoted photocatalytic removal of no under visible light with Bi$_2$MoO$_6$: Indispensable role of superoxide ions, Appl. Catal. B **182**, 316 (2016).

[14] W. Dai, J. Long, L. Yang, S. Zhang, Y. Xu, X. Luo, J. Zou, and S. Luo, Oxygen migration triggering molybdenum exposure in oxygen vacancy-rich ultra-thin Bi$_2$MoO$_6$ nanoflakes: Dual binding sites governing selective CO$_2$ reduction into liquid hydrocarbons, J. Energy Chem. **61**, 281 (2021).

[15] S. Wang, X. Ding, N. Yang, G. Zhan, X. Zhang, G. Dong, L. Zhang, and H. Chen, Insight into the effect of bromine on facet-dependent surface oxygen vacancies construction and stabilization of Bi$_2$MoO$_6$ for efficient photocatalytic no removal, Appl. Catal. B **265**, 118585 (2020).

[16] Y. Sun, H. Wang, Q. Xing, W. Cui, J. Li, S. Wu, and L. Sun, The pivotal effects of oxygen vacancy on Bi$_2$MoO$_6$: Promoted visible light photocatalytic activity and reaction mechanism, Chinese J. Catal. **40**, 647 (2019).

[17] J. Bai, X. Li, Z. Hao, and L. Liu, Enhancement of 3D Bi$_2$MoO$_6$ mesoporous spheres photocatalytic performance by vacancy engineering, J. Colloid Interface Sci. **560**, 510 (2020).

[18] X. Xu, X. Ding, X. Yang, P. Wang, S. Li, Z. Lu, and H. Chen, Oxygen vacancy boosted photocatalytic decomposition of ciprofloxacin over Bi$_2$MoO$_6$: Oxygen vacancy engineering, biotoxicity evaluation and mechanism study, J. Hazard. Mater. **364**, 691 (2019).

[19] T. Jing, Y. Dai, W. Wei, X. Ma, and B. Huang, Near-infrared photocatalytic activity induced by intrinsic defects in Bi$_2$*M*O$_6$ (*M* = W, Mo), Phys. Chem. Chem. Phys. **16**, 18596 (2014).

[20] J. Di, X. Zhao, C. Lian, M. Ji, J. Xia, J. Xiong, W. Zhou, X. Cao, Y. She, H. Liu *et al.*, Atomically-thin Bi$_2$MoO$_6$ nanosheets with vacancy pairs for improved photocatalytic CO$_2$ reduction, Nano Energy **61**, 54 (2019).

[21] Y. Koyama, H. Arai, I. Tanaka, Y. Uchimoto, and Z. Ogumi, Defect chemistry in layered Li*M*O$_2$ (*M* = Co, Ni, Mn, and Li$_{1/3}$Mn$_{2/3}$) by first-principles calculations, Chem. Mater. **24**, 3886 (2012).

[22] G. Kresse and D. Joubert, From ultrasoft pseudopotentials to the projector augmented-wave method, Phys. Rev. B **59**, 1758 (1999).

[23] G. Kresse and J. Hafner, *Ab initio* molecular dynamics for liquid metals, Phys. Rev. B **47**, 558 (1993).

[24] G. Kresse and J. Furthmuller, Efficient iterative schemes for *ab initio* total-energy calculations using a plane-wave basis set, Phys. Rev. B **54**, 11169 (1996).

[25] J. Heyd, G. E. Scuseria, and M. Ernzerhof, Hybrid unctionals based on a screened Coulomb potential, J. Chem. Phys. **118**, 8207 (2003).

[26] K. Lai, W. Wei, Y. Dai, R. Zhang, and B. Huang, DFT calculations on structural and electronic properties of Bi_2MO_6 (M = Cr, Mo, W), Rare Met. **30**, 166 (2011).

[27] R. G. Teller, J. F. Brazdil, R. K. Grasselli, and J. D. Jorgensen, The structure of γ-bismuth molybdate, Bi_2MoO_6, by powder neutron diffraction, Acta Cryst. C **40**, 2001 (1984).

[28] Y. K. Frodason, K. M. Johansen, T. S. Bjørheim, B. G. Svensson, and A. Alkauskas, Zn vacancy as a polaronic hole trap in ZnO, Phys. Rev. B **95**, 094105 (2017).

[29] F. Oba, A. Togo, I. Tanaka, J. Paier, and G. Kresse, Defect energetics in ZnO: A hybrid Hartree-Fock density functional study, Phys. Rev. B **77**, 245202 (2008).

[30] T. R. Mattsson and A. E. Mattsson, Calculating the vacancy formation energy in metals: Pt, Pd, and Mo, Phys. Rev. B **66**, 214110 (2002).

[31] H. J. Monkhorst and J. D. Pack, Special points for Brillouin-zone integrations, Phys. Rev. B **13**, 5188 (1976).

[32] S. Lany and A. Zunger, Accurate prediction of defect properties in density functional supercell calculations, Modell. Simul. Mater. Sci. Eng. **17**, 084002 (2009).

[33] S. Lany and A. Zunger, Assessment of correction methods for the band-gap problem and for finite-size effects in supercell defect calculations: Case studies for ZnO and GaAs, Phys. Rev. B **78**, 235104 (2008).

[34] A. Platonenko, D. Gryaznov, E. A. Kotomin, A. Lushchik, V. Seeman, and A. I. Popov, Hybrid density functional calculations of hyperfine coupling tensor for hole-type defects in $MgAl_2O_4$, Nucl. Instrum. Methods Phys. Res. B **464**, 60 (2020).

[35] H.-P. Komsa, T. T. Rantala, and A. Pasquarello, Finite-size supercell correction schemes for charged defect calculations, Phys. Rev. B **86**, 045112 (2012).

[36] M. Leslie and N. J. Gillan, The energy and elastic dipole tensor of defects in ionic crystals calculated by the supercell method, J. Phys. C: Solid State Phys. **18**, 973 (1985).

[37] D. Zhou, H. Wang, L.-X. Pang, C. A. Randall, and X. Yao, $Bi_2O_3-MoO_3$ binary system: An alternative ultralow sintering temperature microwave dielectric, J. Am. Ceram. Soc. **92**, 2242 (2009).

[38] L.-X. Pang, H. Wang, D. Zhou, and X. Yao, A new temperature stable microwave dielectric with low-firing temperature in Bi_2MoO_6–TiO_2 system, J. Alloys Compd. **493**, 626 (2010).

[39] Z. Zhu, H. Peelaers, and C. G. Van de Walle, Electronic and protonic conduction in $LaFeO_3$, J. Mater. Chem. A **5**, 15367 (2017).

[40] M. Choi, A. Janotti, and C. G. Van de Walle, Native point defects in $LaAlO_3$: A hybrid functional study, Phys. Rev. B **88**, 214117 (2013).

[41] X. Xiang, W. Zhu, T. Lu, T. Gao, Y. Shi, M. Yang, Y. Gong, X. Yu, L. Feng, Y. Wei *et al.*, Density functional theory calculations of point defects and hydrogen isotopes in Li_4SiO_4, AIP Adv. **5**, 107136 (2015).

[42] D. E. Cox, R. J. Cava, D. B. McWhan, and D. W. Murphy, A neutron powder diffraction study of the lithium insertion compound $LiMoO_2$ from 4–440 K, J. Phys. Chem. Solids **43**, 657 (1982).

[43] N. Wooster, The crystal structure of molybdenum trioxide, MoO_3, Z. Kristallogr. Cryst. Mater. **80**, 504 (1931).

[44] G. Malmros, The crystal structure of α-Bi_2O_3, Acta Chem. Scand **24**, 384 (1970).

[45] E. R. Jette and F. Foote, Precision determination of lattice constants, J. Chem. Phys. **3**, 605 (1935).

[46] B. G. Brandt and A. Skapski, A refinement of the crystal structure of molybdenum dioxide, Acta Chem. Scand **21**, 661 (1967).

[47] G. Andersson, A. Magnéli, L. G. Sillén, and M. Rottenberg, On the crystal structure of molybdenum trioxide, Acta Chem. Scand. **4**, 793 (1950).

[48] See Supplemental Material at http://link.aps.org/supplemental/10.1103/PhysRevMaterials.7.045401 for the accessible range of chemical potentials and the formation energies as a function of the Fermi level for Bi_2MoO_6 derived from PBE, the calculated detail of E_F and equilibrium carrier and defect concentrations, the electronic structure of pure and defect Bi_2MoO_6, and E_F, n_0, and the defect concentration as a function of $\Delta\mu_{Mo}$ and $\Delta\mu_o$ in Bi_2MoO_6 along the straight line $A_{HSE}E_{HSE}$ and $A_{HSE}N_{HSE}D_{HSE}$ with or without doping $[A^-] = 10^{18}$ cm^{-3} and $[D^+] = 10^{18}$ cm^{-3}, which includes Refs. [69–73].

[49] P. Gorai, V. Stevanović, and E. S. Toberer, Computationally guided discovery of thermoelectric materials, Nat. Rev. Mater. **2**, 17053 (2017).

[50] J. H. Yang, W. J. Yin, J. S. Park, and S. H. Wei, Self-regulation of charged defect compensation and formation energy pinning in semiconductors, Sci. Rep. **5**, 16977 (2015).

[51] X. Xue, R. Chen, C. Yan, Y. Hu, W. Zhang, S. Yang, L. Ma, G. Zhu, and Z. Jin, Efficient photocatalytic nitrogen fixation under ambient conditions enabled by the heterojunctions of *n*-type Bi_2MoO_6 and oxygen-vacancy-rich *p*-type BiOBr, Nanoscale **11**, 10439 (2019).

[52] J. Buckeridge, T. D. Veal, C. R. A. Catlow, and D. O. Scanlon, Intrinsic point defects and the *n*- and *p*-type dopability of the narrow gap semiconductors GaSb and InSb, Phys. Rev. B **100**, 035207 (2019).

[53] G. Mandel, Self-compensation limited conductivity in binary semiconductors, I. Theory, Phys. Rev. **134**, A1073 (1964).

[54] J. Buckeridge, Equilibrium point defect and charge carrier concentrations in a material determined through calculation of the self-consistent fermi energy, Comput. Phys. Commun. **244**, 329 (2019).

[55] Z. Wang, J. Li, and Y. Q. Fu, Effective *n*-type doping strategy through codoping $Si_{Al} - F_N$ in aluminum nitride, Appl. Phys. Express **7**, 111004 (2014).

[56] A. Martínez-de la Cruz and S. Obregón Alfaro, Synthesis and characterization of γ-Bi_2MoO_6 prepared by co-precipitation: Photoassisted degradation of organic dyes under vis-irradiation, J. Mol. Catal. A: Chem. **320**, 85 (2010).

[57] Y. Shimodaira, Photophysical properties and photocatalytic activities of bismuth molybdates under visible light irradiation, J. Phys. Chem. B **110**, 17790 (2006).

[58] P. Zhang, J.-H. Yang, and X.-G. Gong, Unusual defect properties in multivalent perovskite $Cs_2Au_2I_6$: A first-principles study, Phys. Rev. Mater. **5**, 085405 (2021).

[59] J.-H. Yang, J.-S. Park, J. Kang, W. Metzger, T. Barnes, and S.-H. Wei, Tuning the Fermi level beyond the equilibrium doping

limit through quenching: The case of CdTe, Phys. Rev. B **90**, 245202 (2014).

[60] Y. Zhou, X. Li, L. Xi, and J. Yang, Intrinsic defect study on ternary ABX_2 diamond-like thermoelectric materials and analysis of the density of energy function, J. Materiomics **7**, 19 (2021).

[61] R. Chidthong, S. Insiripong, A. Angnanon, J. Tipwan, R. Rajaramakrishna, and J. Kaewkhao, Photoluminescence properties of Bi_2MoO_6:Dy^{3+} phosphors fabricated by solid state reactions, AIP Conf. Proc. **2279**, 060007 (2020).

[62] B. Han, J. Zhang, P. Li, J. Li, Y. Bian, and H. Shi, Synthesis and luminescence properties of Eu^{3+} doped high temperature form of Bi_2MoO_6, J. Electron. Mater. **44**, 1028 (2015).

[63] E. Gomez, Electrodeposition of nanostructured Bi_2MoO_6@Bi_2MoO_{6-x} homojunction films for the enhanced visible-light-driven photocatalytic degradation of antibiotics Appl, Catal. B **317**, 121703 (2022).

[64] Y. Chen, W. Yang, S. Gao, C. Sun, and Q. Li, Synthesis of Bi_2MoO_6 nanosheets with rich oxygen vacancies by postsynthesis etching treatment for enhanced photocatalytic performance, ACS Appl. Nano Mater. **1**, 3565 (2018).

[65] C. M. C. Vera and R. Aragón, Oxygen partial pressure dependence of electrical conductivity in γ'-Bi_2MoO_6, J. Solid State Chem. **181**, 1075 (2008).

[66] C. M. C. Vera and R. Aragón, Grain boundary and grain interior conduction in γ'-Bi_2MoO_6, Mater. Sci. Eng., B **121**, 187 (2005).

[67] A. Janotti, J. B. Varley, P. Rinke, N. Umezawa, G. Kresse, and C. G. Van de Walle, Hybrid functional studies of the oxygen vacancy in TiO_2, Phys. Rev. B **81**, 085212 (2010).

[68] M. K. Nowotny, T. Bak, and J. Nowotny, Electrical properties and defect chemistry of TiO_2 single crystal. I. Electrical conductivity, J. Phys. Chem. B **110**, 16270 (2006).

[69] L. Weston, L. Bjaalie, K. Krishnaswamy, and C. G. Van de Walle, Origins of *n*-type doping difficulties in perovskite stannates, Phys. Rev. B **97**, 054112 (2018).

[70] L. Ge, Q. Liu, D. Jiang, L. Ding, Z. Wen, Y. Guo, C. Dink, and K. Wang, Oxygen vacancy enhanced photoelectrochemical performance of Bi_2MoO_6/B, N co-doped graphene for fabricating lincomycin aptasensor, Biosens. Bioelectron. **135**, 145 (2019).

[71] D. Segev and S.-H. Wei, Design of Shallow Donor Levels in Diamond by Isovalent-Donor Coupling, Phys. Rev. Lett. **91**, 126406 (2003).

[72] W.-J. Yin, S.-H. Wei, M. M. Al-Jassim, J. Turner, and Y. Yan, Doping properties of monoclinic $BiVO_4$ studied by first-principles density-functional theory, Phys. Rev. B **83**, 155102 (2011).

[73] C. Feng, W.-J. Yin, J. Nie, X. Zu, M. N. Huda, S.-H. Wei, M. M. Al-Jassim, J. A. Turner, and Y. Yan, Strong asymmetrical doping properties of spinel $CoAl_2O_4$, J. Appl. Phys. **111**, 093723 (2012).